4.3　データ同化手法を用いた地震動推定

本項の論文は、SSA（アメリカ地震学会）のオープンアクセス指針に従った上で掲載している。

（Hoshiba, M. and S. Aoki, 2015: Numerical shake prediction for earthquake early warning: data assimilation, real-time shake mapping, and simulation of wave propagation, *Bull. Seismol. Soc. Am.*, **105**, 1324-1338, doi:10.1785/0120140280）

Bulletin of the Seismological Society of America, Vol. 105, No. 3, pp. 1324–1338, June 2015, doi: 10.1785/0120140280

Ⓔ

Numerical Shake Prediction for Earthquake Early Warning: Data Assimilation, Real-Time Shake Mapping, and Simulation of Wave Propagation

by Mitsuyuki Hoshiba and Shigeki Aoki*

Abstract Many of the present earthquake early warning (EEW) systems quickly determine an event's hypocenter and magnitude and then predict strengths of ground motions. The M_w 9.0 Tohoku earthquake, however, revealed some technical issues with such methods: (1) underprediction at large distances due to the large extent of the fault rupture and (2) overprediction because the system was confused by multiple aftershocks that occurred simultaneously. To address these issues, we propose a new concept for EEW, in which the distribution of the present wavefield is estimated precisely in real time (real-time shake mapping) by applying a data assimilation technique, and then the future wavefield is predicted time evolutionally by simulation of seismic-wave propagation. Information on the hypocenter location and magnitude is not necessarily required. We call this method, in which physical processes are simulated from the precisely estimated present condition, numerical shake prediction because of its analogy to numerical weather prediction in meteorology. By applying the proposed method to the 2011 Tohoku earthquake and the 2004 Mid-Niigata Prefecture earthquake (M_w 6.7), we show that numerical shake prediction can precisely and rapidly predict ground motion in real time.

Online Material: Animations as examples of numerical shake prediction.

Introduction

Real-time prediction of strong ground motion is a powerful tool for prevention and mitigation of earthquake disaster, and it has been applied for earthquake early warning (EEW). In recent decades, EEW systems have operated in Mexico and Japan for the general public (Cuéllar *et al.*, 2013, Hoshiba and Ozaki, 2013), and possible use of such systems has been investigated in the United States, Taiwan, the European Union, Turkey, and other countries (e.g., Alcik *et al.*, 2009; Hsiao *et al.*, 2009; Gasparini and Manfredi, 2013; Kuyuk *et al.*, 2014). Many of the present EEW systems first quickly determine the earthquake hypocenter and magnitude and then predict the strengths of ground motions at various sites by applying a ground-motion prediction equation (GMPE) that uses the hypocenter distance and magnitude. In 2007, the Japan Meteorological Agency (JMA) started nationwide operation of an EEW system that basically relies on the quick determination of hypocenter and magnitude (Hoshiba *et al.*, 2008). Hoshiba *et al.* (2011) and Hoshiba and Ozaki (2013) reported on the performance of the JMA EEW system for the 2011 Off the Pacific Coast of Tohoku earthquake (M_w 9.0 Tohoku earthquake): an EEW was issued more than 15 s earlier than the start of the strong ground shaking in the Tohoku district (relatively near distance from the epicenter). The M_w 9.0 earthquake, however, revealed two important technical issues with the method: it underpredicted ground motion at large distances because of the large extent of the fault rupture, and it sometimes overpredicted because the system was confused by multiple aftershocks that occurred simultaneously.

In the present JMA EEW method, rupture length L (in kilometers) is estimated from the magnitude M using the empirical relation $\log_{10} L = 0.5M–1.85$ (Utsu, 2001), $L/2$ is then substituted from the hypocentral distance to estimate the shortest distance from the rupture for application of the GMPE. During the Tohoku earthquake, the JMA EEW system underestimated the magnitude as 8.1. This underestimation led to the underestimation of the rupture length and thus to the underprediction of strength of ground motion in the Kanto region (relatively far from the epicenter). After the mainshock, aftershock activity was quite high for several weeks. When multiple aftershocks occurred simultaneously over this wide source region, the system became confused;

*Now at The Japan Meteorological Agency, Ohte-machi 1-3-4, Chiyoda, Tokyo 100-8122, Japan.

the multiple small events were interpreted as a large earthquake, and, as a result, the system did not always correctly determine the hypocenter and magnitude. This incorrect estimation sometimes led to overprediction of the strength of ground motion and, therefore, false warnings.

Several methods have been proposed to address the issue arising from the extent of rupture during large earthquakes (e.g., Böse *et al.*, 2008, 2012; Irikura and Kurahashi, 2011; Yamada, 2013). To address the problem of multiple simultaneous events, Liu and Yamada (2014) recently proposed applying a Bayesian approach to identify the sources. These methods still focus on rapid estimation of source parameters (e.g., hypocenter, magnitude, and source extent). At present, many EEW techniques are based on rapid estimation of source parameters, including the extent of the source region. Certain fundamental questions arise, specifically, "Is rapid estimation of the source parameters the only possible approach for EEW?" and "Is precise estimation of the source parameters the only possible method for improving the precision of EEW?" In this article, we explore another EEW concept, one that does not require the rapid estimation of source parameters.

Instead of the rapid estimation of the source parameters, Hoshiba (2013a) recently proposed a new technique that applies a boundary integral equation, such as the Kirchhoff–Fresnel integral theorem, in which ground motion is predicted from ground-motion observation at front stations in the direction of incoming seismic waves. This method enables us to predict ground motion without information on the earthquake hypocenter and magnitude, although to apply the method, it is necessary to estimate (or assume) the direction of the seismic-wave propagation.

Data assimilation is a technique for precise estimation of the present condition (Kalnay, 2003; Awaji *et al.*, 2009). It is widely used for rocket and robot control in mechanical engineering and for numerical weather prediction and oceanography in geophysics. In particular, application of the method for numerical weather prediction has improved the precision of routine weather forecasts in recent decades. The data assimilation technique is applied to estimate precisely the initial condition in the simulation of atmospheric dynamics.

In this article, we investigate a method of predicting ground motion in real time for EEW. In this method, the prediction of the future distribution of ground motion is based on a physical process of wave propagation, without first determining source parameters such as the earthquake hypocenter and magnitude. We apply a data assimilation technique to estimate precisely the initial condition (i.e., the present distribution of seismic ground motion). For simulation of seismic-wave propagation, radiative transfer theory (RTT) is used instead of the Kirchhoff–Fresnel integral theorem. RTT is based on a ray theoretical approach using high-frequency approximation (Sato *et al.*, 2012), and it requires much less computational time than the Kirchhoff–Fresnel integral. Because our proposed method is based on the simulation of time evolution of a physical process from the precisely estimated present condition, we call the method numerical shake prediction, analogous to numerical weather prediction in meteorology, in which present atmospheric conditions (i.e., the distribution of pressure, temperature, wind strength, wind direction, and so on) are precisely estimated by data assimilation and then future conditions are predicted from the time evolution of the atmosphere dynamics.

Because the method does not require a trigger and phase pickup (reading of the arrival time of the P and S phases), it is possible to operate the system continuously regardless of whether earthquakes are occurring or not. When no ground motion is observed, the system predicts that there will be no ground motion anywhere in the future. Continuous operation minimizes the workload fluctuation, which is important for actual application to EEW.

We then apply the proposed method to actual data using as examples the 2011 Tohoku earthquake (M_w 9.0) and the 2004 Mid-Niigata Prefecture earthquake (M_w 6.7). The proposed method enables us to predict ground motion more precisely in real time than methods based on the rapid estimation of hypocenter and magnitude.

Methods

In the proposed method, the present wavefield is first estimated using a data assimilation technique, and then RTT is applied in the simulation of wave propagation to estimate the future wavefield (Fig. 1).

Data Assimilation

Data assimilation technique is widely used in numerical weather prediction, oceanography, and rocket control for precise estimation of the present condition (Kalnay, 2003; Awaji *et al.*, 2009). The technique is a kind of spatial interpolation, the application of which has been made possible by the development of computers. Figure 1 (upper part) illustrates the data assimilation procedure, in which the spatial distribution of the wavefield is estimated from not only actual observations, but also the simulation of wave propagation based on wave propagation physics.

To estimate the distribution of wavefield at a certain elapsed time, one of the simplest methods is to draw contours of the observed data. However, that approach does not take into account wave propagation. By considering wave propagation physics, we can anticipate the distribution of the wavefield at $t = t_n$ from its distribution one time step previously ($t = t_{n-1} = t_n - \Delta t$, in which Δt is the elapse time interval). By combining the anticipated distribution from one time step before ($t = t_{n-1}$) with the actual observation at $t = t_n$, we can estimate the wavefield more precisely. That is the basic principle of the data assimilation technique. For data assimilation techniques, several methods have been proposed, including an optimal interpolation method and the Kalman filter method. In this article, we apply an optimal interpolation method, following Awaji *et al.* (2009).

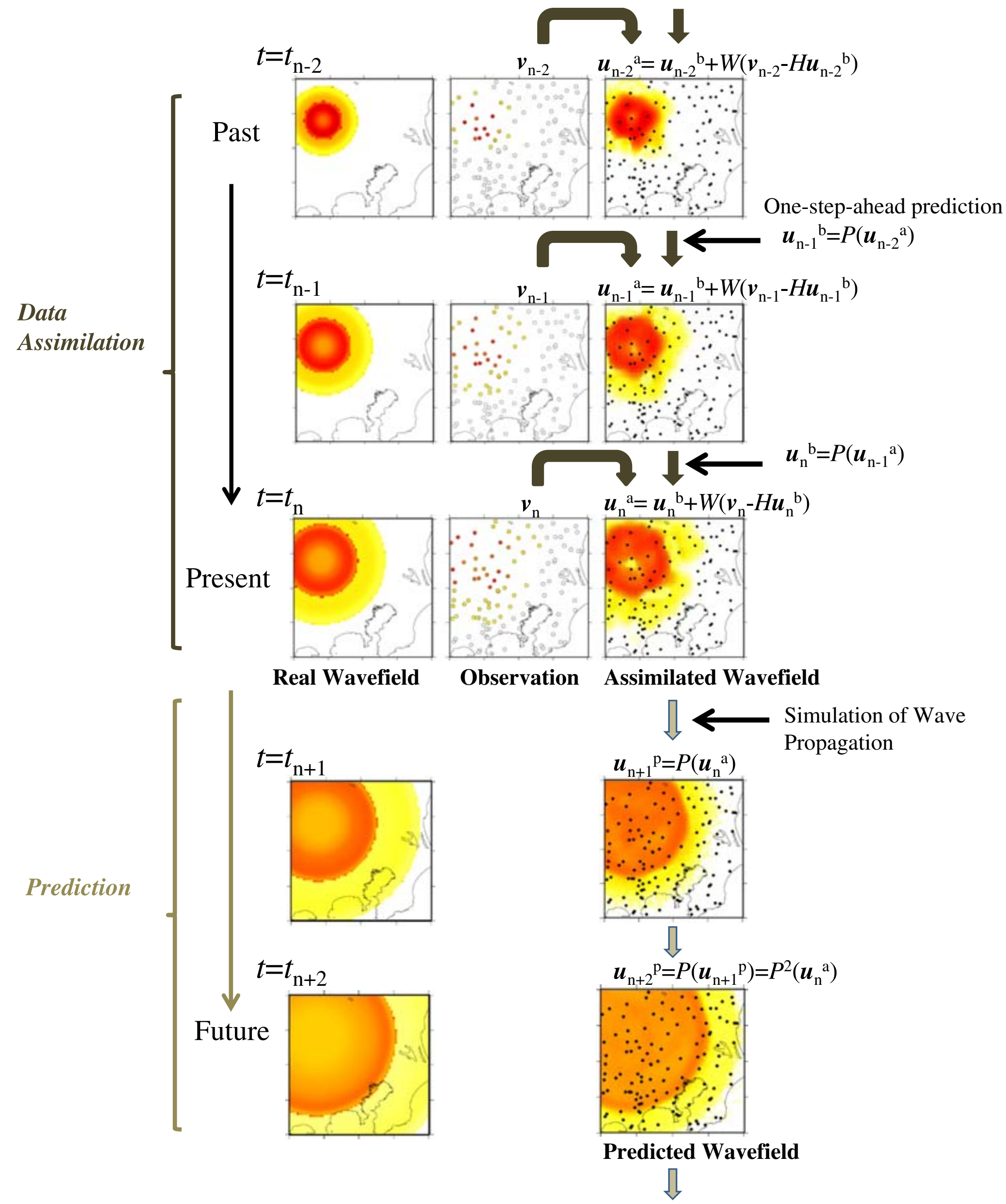

Figure 1. Schematic illustration of the proposed method from data assimilation to prediction. In the data assimilation process, one-step-ahead prediction $\mathbf{u}_n^b = P(\mathbf{u}_{n-1}^a)$ is combined with the actual observation $\mathbf{v}_n$ to estimate the present situation, $\mathbf{u}_n^a = \mathbf{u}_n^b + \mathbf{W}(\mathbf{v}_n - \mathbf{H}\mathbf{u}_n^b)$. In the prediction process, one-step-ahead prediction is repeatedly applied to predict the future situation. In the assimilated and predicted wavefields, small dots indicate the locations of KiK-net stations of the National Research Institute for Earth Science and Disaster Prevention and stations of the Japan Meteorological Agency (JMA) network in the Kanto district, Japan. The color version of this figure is available only in the electronic edition.

Let $\mathbf{u}_n$ indicate the wavefield in the model space at time t_n, in which $\mathbf{u}_n = (u_{n1}, u_{n2,} u_{n3,} \ldots, u_{ni,} \ldots, u_{nI})$ and i indicates ith elements in the model space of the simulation of wave propagation. Examples of elements are locations, components, and types of measurements (acceleration, velocity, or displacement). In the case of locations, they are usually located on grid points on a map (Fig. 2). Let the total number of elements be I. When $\mathbf{u}_{n-1}$ is given, we can image $\mathbf{u}_n$ by a simulation of wave propagation. Let P be a prediction operator of one time step (i.e., P represents the time evolution of wave propagation from time t_{n-1} to time t_n):

$$\mathbf{u}_n = P(\mathbf{u}_{n-1}); \qquad (1)$$

for example, the 1D advection equation $\partial u/\partial t + v\partial u/\partial x = 0$ is approximated as $(u_{ni} - u_{n-1i})/\Delta t \approx -v(u_{n-1i} - u_{n-1i-1})/\Delta x$. Therefore, P is expressed as $u_{ni} \approx u_{n-1i} - v(u_{n-1i} - u_{n-1i-1})\Delta t/\Delta x$, and $\mathbf{u}_n$ is predicted

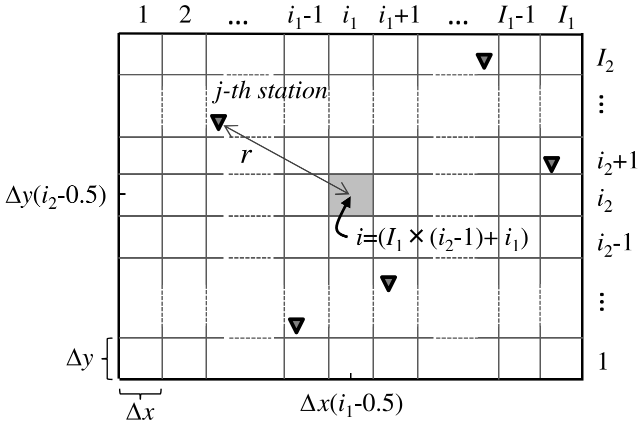

Figure 2. Relation of grid space with the ith element of model space. The location of element $i = (I_1 \times (i_2 - 1) + i_1)$ in the grid space is given by $(x, y) = (\Delta x(i_1 - 0.5), \Delta y(i_2 - 0.5))$, in which the grid space is divided horizontally by I_1 and vertically by I_2. The reverse triangles indicate the locations of observation stations.

from $\mathbf{u}_{n-1}$. To discriminate $\mathbf{u}_n$ between before and after the combination with the actual observation, the distributions before and after are denoted $\mathbf{u}_n^b$ and $\mathbf{u}_n^a$, respectively. P is applied to the distribution after the combination at one time step before, $n-1$; thus equation (1) is expressed as

$$\mathbf{u}_n^b = P(\mathbf{u}_{n-1}^a). \tag{2}$$

The process expressed by equation (2) is called one-step-ahead prediction in the data assimilation technique.

Let $\mathbf{v}_n = (v_{n1}, v_{n2}, v_{n3}, \dots, v_{nj}, \dots, v_{nJ})$ be the actual observation in observational space at time t_n, in which $v_{\mathrm{n}j}$ means the observed data of the jth element. Let the total number of observed elements be J. Usually I (number of grids) is much larger than J (number of observation points). Data assimilation is expressed as

$$\mathbf{u}_n^a = \mathbf{u}_n^b + \mathbf{W}\Delta\mathbf{v}_n, \tag{3}$$

in which $\Delta\mathbf{v}_n = \mathbf{v}_n - \mathbf{H}\mathbf{u}_n^b$. Here, $\mathbf{H}$ is the $J \times I$ matrix called the observation matrix, and it means the interpolation of grid points onto the location of the observation points. Therefore, $\Delta\mathbf{v}_n$ is the difference between the one-step-ahead prediction and the actual observation at time t_n. $\mathbf{W}$ is the $I \times J$ matrix called the weight matrix, and $\mathbf{W}\Delta\mathbf{v}$ indicates the correction of the one-step-ahead prediction in the wave propagation simulation. From $\mathbf{u}_n^a$, $\mathbf{u}_{n+1}^b$ is obtained from equation (2). Iterative application of equations (2) and (3) produces a time-evolutional estimation of wavefield. The process on the right side in Figure 1 indicates repeated application of a one-step-ahead prediction, that is, the simulation of wave propagation. In the data assimilation technique, actually observed data are included in the simulation at each time step; that is, actual data are assimilated in the simulation process.

The parameter setting for $\mathbf{W}$ is important in data assimilation. In the optimal interpolation method, $\mathbf{W}$ is constant irrespective of time n, though in the Kalman filter method it changes with increasing n. Matrix $\mathbf{W}$ is expressed in relation to the errors in one-step-ahead prediction (background error) and the errors in observations (observational error),

$$\mathbf{W} = \mathbf{B}\mathbf{H}^T(\mathbf{R} + \mathbf{H}\mathbf{B}\mathbf{H}^T)^{-1}, \tag{4}$$

in which $\mathbf{B}$ and $\mathbf{R}$ are the background error covariance matrix and the observational error covariance matrix, respectively. Here, the background error and the observational error are defined as the error of $\mathbf{u}_n^b$ and $\mathbf{v}_n$, respectively, which are deviations from the unknown true wavefield. Fluctuation that has a size that is smaller than the grid interval of the model space is included in the observational error as well as instrumental error. $\mathbf{HBH}^{\mathrm{T}}$ is a $J \times J$ matrix and indicates the projection of the background error onto observation points

$$\begin{aligned}\mathbf{HBH}^T &= \begin{pmatrix} b_{11}^h & b_{12}^h & \dots & b_{1J}^h \\ b_{21}^h & b_{22}^h & \dots & b_{2J}^h \\ \dots & \dots & \dots & \dots \\ b_{J1}^h & b_{J2}^h & \dots & b_{JJ}^h \end{pmatrix} \\ &= \begin{pmatrix} \sigma_1^b & 0 & \dots & 0 \\ 0 & \sigma_2^b & \dots & 0 \\ \dots & \dots & \dots & \dots \\ 0 & 0 & \dots & \sigma_J^b \end{pmatrix} \begin{pmatrix} \mu_{11}^b & \mu_{12}^b & \dots & \mu_{1J}^b \\ \mu_{21}^b & \mu_{22}^b & \dots & \mu_{2J}^b \\ \dots & \dots & \dots & \dots \\ \mu_{J1}^b & \mu_{J2}^b & \dots & \mu_{JJ}^b \end{pmatrix} \\ &\times \begin{pmatrix} \sigma_1^b & 0 & \dots & 0 \\ 0 & \sigma_2^b & \dots & 0 \\ \dots & \dots & \dots & \dots \\ 0 & 0 & \dots & \sigma_J^b \end{pmatrix},\end{aligned} \tag{5}$$

in which b_{kj}^h indicates the covariance of the background error between the kth and jth elements in model space. σ_j^b denotes the standard deviation of the background error of the jth element, and μ_{kj}^b represents the correlation of the background error between the kth and jth elements. Matrix $\mathbf{R}$ is represented as

$$\begin{aligned}\mathbf{R} &= \begin{pmatrix} r_{11} & r_{12} & \dots & r_{1J} \\ r_{21} & r_{22} & \dots & r_{2J} \\ \dots & \dots & \dots & \dots \\ r_{J1} & r_{J2} & \dots & r_{JJ} \end{pmatrix} \\ &= \begin{pmatrix} \sigma_1^o & 0 & \dots & 0 \\ 0 & \sigma_2^o & \dots & 0 \\ \dots & \dots & \dots & \dots \\ 0 & 0 & \dots & \sigma_J^o \end{pmatrix} \begin{pmatrix} \mu_{11}^o & \mu_{12}^o & \dots & \mu_{1J}^o \\ \mu_{21}^o & \mu_{22}^o & \dots & \mu_{2J}^o \\ \dots & \dots & \dots & \dots \\ \mu_{J1}^o & \mu_{J2}^o & \dots & \mu_{JJ}^o \end{pmatrix} \\ &\times \begin{pmatrix} \sigma_1^o & 0 & \dots & 0 \\ 0 & \sigma_2^o & \dots & 0 \\ \dots & \dots & \dots & \dots \\ 0 & 0 & \dots & \sigma_J^o \end{pmatrix},\end{aligned} \tag{6}$$

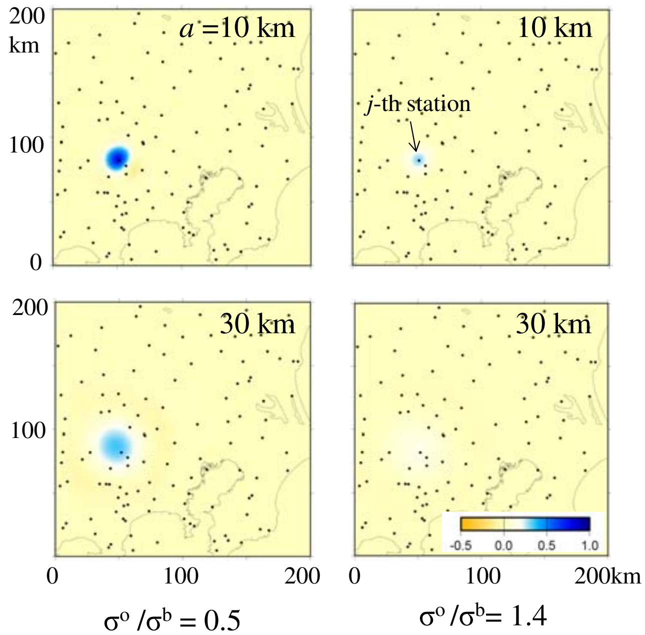

Figure 3. Distribution of w_{ij} for correlation distance $a = 10$ and 30 km and for two different ratios of the observational error to the background error (σ^o/σ^b). Here, w_{ij} is the element in the ith row and the jth column of weight matrix $\mathbf{W}$, in which i and j indicate grids and stations, respectively. The color version of this figure is available only in the electronic edition.

in which σ_j^o denotes the standard deviation of the observational error of the jth element, and μ_{kj}^o represents the correlation of the observational error between the kth and jth elements. $\mathbf{BH}^T$ is an $I \times J$ matrix, and

$$\mathbf{BH}^T = \begin{pmatrix} b_{11}^g & b_{12}^g & \dots & b_{1J}^g \\ b_{21}^g & b_{22}^g & \dots & b_{2J}^g \\ \dots & \dots & b_{ij}^g & \dots \\ b_{I1}^g & b_{I2}^g & \dots & b_{IJ}^g \end{pmatrix}, \quad (7)$$

in which b_{ij}^g indicates the covariance of the background error between the ith element in model space and the jth element in observational space. b_{ij}^g is calculated from the standard deviation of the background error at the ith element in model space σ_i^b, that at the jth element in observational space σ_j^b, and the correlation of background error between the ith element in model space and the jth element in observational space μ_{ij}^b:

$$b_{ij}^g = \mu_{ij}^b \sigma_i^b \sigma_j^b. \quad (8)$$

When the background error, the observation error, and their correlations are determined, the weight matrix $\mathbf{W}$ is calculated.

Figure 3 illustrates an example of $\mathbf{W}$, in which the i elements are grid locations and the j elements are stations locations. Let w_{ij} be the component in the ith row and the jth column of $\mathbf{W}$. The distribution of w_{ij} for a certain j is plotted in Figure 3. The correlation of background error μ_{ij}^b is assumed to be a Gaussian-type correlation, that is, $\mu_{ij}^b = \exp(-r^2/a^2)$, in which r is the distance between the ith grid and the jth station and a is the correlation distance. No correlations are assumed for observational error at different locations; that is, $\mu_{kj}^o = 0\,(k \neq j)$ or $= 1\ (k = j)$. In this article, standard deviations of the background error σ^b are assumed to be the same, independent of i or j, and those of the observational error σ^o are also assumed not to depend on j. Thus, in determination of w_{ij}, the ratio σ^o/σ^b is used instead of the individual values of σ^o and σ^b. As shown in Figure 3, w_{ij} is distributed at a distance of a around the jth station. This means that in equation (3), the correction $\mathbf{W}\Delta\mathbf{v}$ is applied in a wider area around the jth station with increasing a. When the observational error is smaller than the background error (i.e., $\sigma^o/\sigma^b < 1$), the observation is more reliable than one-step-ahead prediction, and w_{ij} is larger than it is when $\sigma^o/\sigma^b > 1$.

Matrix $\mathbf{W}$ has a form of (background errors)/(observational errors + background errors) as shown in equation (4). The case in which observational errors are assumed to be much larger than background errors $\sigma_j^o \gg \sigma_j^b$ leads to $\mathbf{W} \approx 0$ and then $\mathbf{u}_n^a \approx \mathbf{u}_n^b$. Iterative application of equations (2) and (3), therefore, results in just the simulation of wave propagation, because the observations have no effect. In contrast, the case in which background errors are assumed to be much larger than observational errors ($\sigma_j^b \gg \sigma_j^o$) corresponds to the case in which the contours of the actual observations are drawn independently at each time step, because the one-step-ahead prediction has little effect in equation (3).

As shown in Figure 1, the present distribution $\mathbf{u}_n^a$ is estimated using all past observations $\mathbf{v}_{n-1}$, $\mathbf{v}_{n-2}$, $\mathbf{v}_{n-3}, \dots$ in addition to the present observation $\mathbf{v}_n$. Real-time application of the data assimilation technique enables us to estimate $\mathbf{u}_n^a$ in real time, which corresponds to the real-time version of ShakeMap proposed by Wald *et al.* (2006). Although the standard ShakeMap is obtained by interpolation of the observed strength of ground motion after an earthquake (Wald *et al.*, 2006), taking the difference of site amplification into account, the real-time shake map is created in real time from both observations and simulations of wave propagation by employing a data assimilation technique.

Seismometers are usually deployed at the ground surface. It is thus impossible to apply data assimilation for a deep underground wavefield. Although seismic waves propagate in 3D space, we apply data assimilation technique in 2D space in this article. We discuss the difference between 2D and 3D spaces in the Discussion section.

Radiative Transfer Theory for Simulation of Wave Propagation

To apply the data assimilation technique to seismic-wave propagation, it is necessary to simulate wave propagation, as shown in equations (1) and (2). For seismological applications, some simulation methods have been proposed, such as the finite-difference method, finite-element method, boundary integral equation method, and so on. RTT is based on the ray theoretical approach, so that it is an approximation for high-frequency waves. In RTT, peaks and troughs of waveforms are neglected, and energy propagation is considered instead of wave propagation. RTT is based on the Boltzmann equation (Ishimaru, 1997) and has been widely used to interpret seismogram envelopes of high-frequency seismic waves (Sato *et al.*, 2012). Because of the approximation, much less computational time is required compared with the finite-difference method and boundary integral equation method. Less computation time is important in EEW application, because the computation must be completed as quickly as possible before the actual ground motion arrives.

RTT represents scattering and attenuation processes while neglecting interference effect (Sato *et al.*, 2012), and RTT is expressed in 2D space as follows:

$$\begin{aligned}\dot{f}(\mathbf{x},t:\theta) &+ V(\mathbf{x})\mathbf{s}_\theta \nabla f(\mathbf{x},t:\theta)\\ &= -[g_s(\mathbf{x}) + h_s(\mathbf{x})]V(\mathbf{x})f(\mathbf{x},t:\theta)\\ &\quad + \frac{V(\mathbf{x})}{2\pi}\int g(\mathbf{x},\theta-\theta')f(\mathbf{x},t:\theta')d\theta', \qquad (9)\end{aligned}$$

in which f is energy density at location $\mathbf{x}$ and time t traveling in direction θ; $\mathbf{s}_\theta$ is the unit vector with direction θ; $V(\mathbf{x})$ is the velocity of P wave (V_P) or S wave (V_S) at $\mathbf{x}$; $g(\mathbf{x},\theta)$ is the scattering strength at $\mathbf{x}$ with the scattering angle θ; and

$$g_s(\mathbf{x}) = \frac{1}{2\pi}\int_0^{2\pi} g(\mathbf{x},\theta)d\theta. \qquad (10)$$

Here, it is assumed that scattering does not cause wave conversion ($P \to S$ or $S \to P$). Attenuation due to intrinsic absorption at $\mathbf{x}$ is denoted by $h_s(\mathbf{x})$. In this article, we assume for simplicity that the velocity structure and the attenuation structure are homogeneous; thus, velocity, scattering strength, and intrinsic absorption are independent of $\mathbf{x}: V(\mathbf{x}) = V_0$, $g_s(\mathbf{x}) = g_0$, and $h_s(\mathbf{x}) = h_0$; isotropic scattering is also assumed. Then equation (9) is expressed as

$$\begin{aligned}\dot{f}(\mathbf{x},t:\theta) &+ V_0\mathbf{s}_\theta\nabla f(\mathbf{x},t:\theta)\\ &= -(g_0+h_0)V_0 f(\mathbf{x},t:\theta) + \frac{V_0}{2\pi}\int g_0 f(\mathbf{x},t:\theta')d\theta'. \qquad (11)\end{aligned}$$

The left side of equation (11) represents advection, the first term on the right side means attenuation, and the second term represents scattering from direction θ' to θ. Because the first term on the left side is the differential of f with respect to time, equation (11) means that it is possible to predict future f provided the spatial and directional distribution of f is known precisely in the present. Note that information on the earthquake hypocenter and magnitude is not required for this prediction.

Application of RTT to Data Assimilation

In RTT, information on the direction of propagation θ is required. However, in actual seismic observation, it is not easy to estimate the direction of propagation in real time. Such estimation might be possible if data from many arrays of seismometers were available, but an observation using many arrays is not so realistic at present. Instead, what we can compare with the actual observations is the integral of f with respect to direction, then $\mathbf{u}_n^b$ is given as

$$u_{ni}^{\mathrm{b}} = F(\mathbf{x}_i, t_n) = \int_0^{2\pi} f^b(\mathbf{x}_i, t_n:\theta)d\theta, \qquad (12)$$

in which u_{ni}^{b} is the ith component of $\mathbf{u}_n^b$ vector, F represents the space–time distribution of the energy density, and $\mathbf{x}_i$ is the location of the center of the ith grid. The superscript b in f^b means it is before the combination with the actual observation in data assimilation (hereinafter, the superscript a in f^a means it is after the combination). After applying one-step-ahead prediction, $\mathbf{u}_n^b$ is obtained as shown in equation (2). Combined with the actual observation $\mathbf{v}_n$, $\mathbf{u}_n^a$ is obtained as shown in (3) using data assimilation.

When the ith component of $\mathbf{u}_n^a$ is smaller than u_{ni}^{b} (i.e., $u_{ni}^a < u_{ni}^{\mathrm{b}}$), overprediction occurs at the ith grid. To make the energy density at the grid i consistent with $\mathbf{u}_{ni}^a$, it is necessary to reduce the energy at the location of the ith grid. The energy is reduced as

$$f^a(\mathbf{x}_i,t_n:\theta) = u_{ni}^a/u_{ni}^b f^b(\mathbf{x}_i,t_n:\theta), \quad \text{when } u_{ni}^a < u_{ni}^b. \qquad (13)$$

On the other hand, when $u_{ni}^a > u_{ni}^b$ underprediction occurs, it is necessary to add energy in the amount of $(u_{ni}^a - u_{ni}^b)$ at the location of the ith grid. New energy of $(u_{ni}^a - u_{ni}^b)$ is radiated from the ith grid. When the radiation is assumed to be isotropic, f^a is given as

$$\begin{aligned}f^a(\mathbf{x}_i,t_n:\theta) &= f^b(\mathbf{x}_i,t_n:\theta) + (u_{ni}^a - u_{ni}^b)/2\pi\\ &\text{when } u_{ni}^a > u_{ni}^b. \qquad (14)\end{aligned}$$

Here, $(u_{ni}^a - u_{ni}^b)W_P/(W_S + W_P)$ is radiated as P-wave energy having $V_0 = V_P$, and $(u_{ni}^a - u_{ni}^b)W_S/(W_S + W_P)$ as S-wave energy, having $V_0 = V_S$, and $W_S/W_P = 3/2(V_P/V_S)^5$ is assumed for the ratio of radiated S-to-P-wave energy (Sato *et al.*, 2012). Although the new energy $(u_{ni}^a - u_{ni}^b)$ is radiated isotropically from $\mathbf{x}_i$ for a single grid, radiation from many grids makes plane waves as data assimilation is applied repeatedly, when the plane wave is incident from outside of the model space. This is similar to an image based on Huygen's principle: in the case of plane wave incidence, isotropic radiation of many virtual secondary sources located on the wavefront line makes a new future wavefront that is also a plane wave.

One-step-ahead prediction is conducted from $f^a(\mathbf{x}_i, t_{n-1}:\theta)$ based on equation (11), and $f^b(\mathbf{x}_i,t_n:\theta)$ is obtained. Applying equation (12), $\mathbf{u}_n^b$ is estimated. By combining $\mathbf{u}_n^b$ with the actual observation $\mathbf{v}_n$, $\mathbf{u}_n^a$ is obtained, as shown in equation (3) in the data assimilation technique. Then

$f^a(\mathbf{x}_i, t_n : \theta)$ is estimated using equations (13) or (14). These steps are repeated to estimate the precise distribution of the strength of the ground motion.

Let model space $\mathbf{x}$ be divided by I_1 horizontally and by I_2 vertically, with increments Δx and Δy, respectively, on the map image (Fig. 2). The total number of grids is $I = I_1 \times I_2$, and the grid number is given by $i = I_2 \times (i_1 - 1) + i_2$, in which $i_1 = 1, 2, 3, \ldots, I_1$ and $i_2 = 1, 2, 3, \ldots, I_2$. For example, the $(I_1 \times (i_2 - 1) + i_1)$th component of $\mathbf{u}_n$ is given by F at location $\mathbf{x}_i = (\Delta x(i_1 - 0.5), \; \Delta y(i_2 - 0.5))$. Because F represents the energy density, $F(\mathbf{x}, t)$ has been assumed to be proportional to the squared amplitude of seismic waves in many previous studies (e.g., Fehler *et al.*, 1992; Hoshiba *et al.*, 2001). In this study as well, $F(\mathbf{x}, t)$ is assumed to be proportional to the envelope of $A_{\mathrm{NS}}^2(\mathbf{x}, t) + A_{\mathrm{EW}}^2(\mathbf{x}, t) + A_{\mathrm{UD}}^2(\mathbf{x}, t)$, in which A_{NS}, A_{EW}, and A_{UD} are the band-pass-filtered three-component seismograms of ground motion observed at location $\mathbf{x}$.

Particle Method of RTT Simulation

For efficient calculation of RTT simulation, a particle method based on the Monte Carlo technique has been widely used in recent decades (e.g., Gusev and Abubakirov, 1987; Hoshiba, 1991, 1995, 1997; Yoshimoto, 2000). In this method, the propagation of wave energy is simulated by the movement of a very large number of particles. In this article, we follow the direct-simulation Monte Carlo method proposed by Yoshimoto (2000). Instead of the Eulerian representation expressed in equation (11), we use the Lagrangian representation

$$\begin{aligned}\frac{Df(\mathbf{x}, t:\theta)}{Dt} &= -(g_0 + h_0)V_0 f(\mathbf{x}, t:\theta) + \frac{V_0}{2\pi}\int g_0 f(\mathbf{x}, t:\theta')d\theta' \\ &= -g_0 V_0 f(\mathbf{x}, t:\theta) + \frac{V_0}{2\pi}\int g_0 f(\mathbf{x}, t:\theta')d\theta' \\ &\quad - h_0 V_0 f(\mathbf{x}, t:\theta). \qquad (15)\end{aligned}$$

First, let us consider the case of $h_0 = 0$, which means no absorption. The first term on the right side means that the energy propagating in direction θ is attenuated by scattering in proportion to f. The energy density f decreases exponentially as travel distance increases. The second term is the contribution of energy changing direction from θ' into θ. This physical process is simulated by many particles through a probability process (Fig. 4): the probability that energy travels for time Δt without scattering is $\exp(-g_0 V_0 \Delta t)$. The probability that scattering occurs during the time interval is given by $1 - \exp(-g_0 V_0 \Delta t)$, which is approximated as $g_0 V_0 \Delta t$ when $g_0 V_0 \Delta t \ll 1$. When scattering occurs, the probability density of scattering from θ' toward θ is $1/(2\pi)$, because scattering is assumed to be isotropic. These processes are simulated by using very large number of particles.

Let the number of particles be M, and let $\mathbf{X}_{n,m}$ be the location of the mth particle at time n. When it is traveling in direction θ_m, the particle is expected to move by $V_0 \Delta t \mathbf{s}_{\theta m}$ over the time interval Δt, if scattering does not occur. In contrast, if scattering occurs, the particle changes direction. Let R_1 and R_2 be independent uniform random variables between 0 and 1. When $R_1 \geq g_0 V_0 \Delta t$ (i.e., no scattering), the particle is located at $\mathbf{X}_{n,m} = \mathbf{X}_{n-1,m} + V_0 \Delta t \mathbf{s}_{\theta m}$ at the next time step. When $R_1 < g_0 V_0 \Delta t$ (i.e., with scattering), the new traveling direction is determined from $\theta_1 = (2\pi)R_2$, and then the particle is located at $\mathbf{X}_{n,m} = \mathbf{X}_{n-1,m} + V_0 \Delta t \mathbf{s}_1$ after Δt, in which $\mathbf{s}_1$ is the unit vector with direction θ_1. At the next time step, $\theta_m = \theta_1$ is used as the traveling direction.

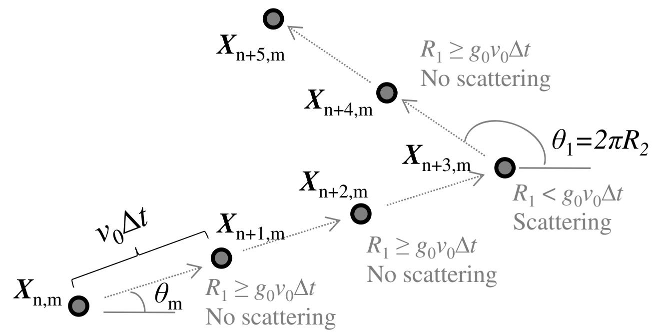

Figure 4. Propagation of an energy particle in radiative transfer theory (RTT). If the mth particle is located at $\mathbf{X}_{n,m}$ at lapse time n, it will be at $\mathbf{X}_{n+1,m} = \mathbf{X}_{n,m} + V_0 \Delta t \mathbf{s}_{\theta m}$ at $n+1$ in the no-scattering case. In the scattering case, the new propagation direction is given by $2\pi R_2$, in which R_2 is a random variable between 0 and 1. In this article, isotropic scattering is assumed.

The third term on the left side of equation (15) represents attenuation due to absorption. When the mth particle has energy $q_{n,m}$ at time n, the energy is attenuated as follows:

$$q_{n,m} = q_{n-1,m}\exp(-h_0 V_0 \Delta t) \approx q_{n-1,m}(1 - h_0 V_0 \Delta t), \quad (16)$$

with increasing n, in which $h_0 V_0 \Delta t \ll 1$ is assumed. The energy of the particle is attenuated as the elapse time increases, whether or not scattering occurs. In this article, because h_0 is assumed to be homogeneous (i.e., independent of $\mathbf{x}$), the amount of attenuation of each particle is the same for all m.

From the present situation of location $\mathbf{X}_{n,m}$, direction θ_m, and energy $q_{n,m}$, we can estimate the future situation after Δt. The same procedure is repeated for $m = 1, 2, 3, \ldots, M$. This is one-step-ahead prediction conducted using the particle method. The distribution of particles represents the spatial, temporal, and directional distribution of $f(\mathbf{x}, t : \theta)$. To minimize fluctuations in the number of particles M among different time step n, we reconstruct the particles for each time step during data assimilation. In the ith grid at time t_n, $\mathrm{Int}(M u_{ni}^a / \Sigma_i^I u_{ni}^a)$ particles are assigned to represent the wavefield after the reconstruction, where Int means conversion to the nearest integer value.

Prediction

Once the present situation $\mathbf{u}_n^a$ has been estimated precisely by the data assimilation technique, we progress to prediction of the future situation (Fig. 1, lower part). Because future observations are not yet available for data assimilation,

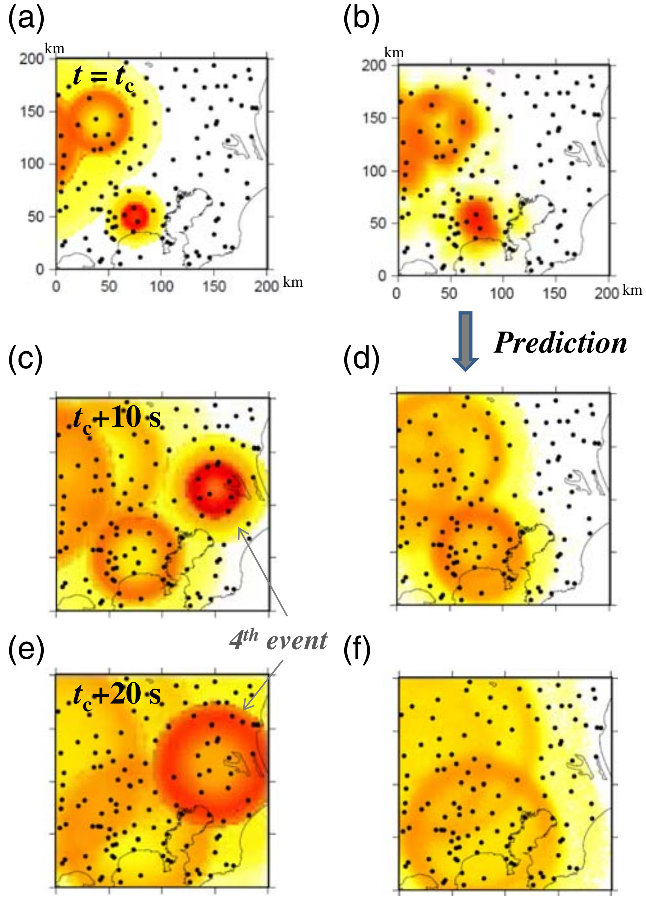

Figure 5. Schematic illustration for comparison of predicted and synthesized (i.e., real) distributions: (a), (c), and (e) indicate the synthesized distributions at $t = t_c$, $t_c + 10$ s, and $t_c + 20$ s, respectively, and (b) shows the assimilated distribution at $t = t_c$. From (b), distributions of (d) and (f) are predicted for $t = t_c + 10$ s and $t = t_c + 20$ s, respectively. Note that the fourth event has not occurred at $t = t_c$. The color version of this figure is available only in the electronic edition.

the wave propagation physics are calculated without data assimilation. Thus, wave propagation is simulated from the initial condition $\mathbf{u}_n^a$. In this article, RTT is again adopted to simulate wave propagation for prediction. The same procedures as described in the Particle Method of RTT Simulation section are applied; that is, $\mathbf{u}_{n+1}^p = P(\mathbf{u}_n^a)$, in which the superscript p of $\mathbf{u}_{n+1}$ means the predicted situation at time $n + 1$. Repeating this process,

$$\mathbf{u}_{n+k}^p = P(\mathbf{u}_{n+k-1}^p) = P^2(\mathbf{u}_{n+k-2}^p) = \ldots = P^{k-1}(\mathbf{u}_{n+1}^p) = P^k(\mathbf{u}_n^a) \tag{17}$$

enables us to predict the situation after k time steps.

Figure 5 schematically shows predictions for four events that occur in succession at a focal depth of 10 km, where the S and P waves propagate at velocities of 3 and 5.1 km/s, respectively. One event occurs outside the range of the map. Figure 5b shows the present situation $\mathbf{u}_n^a$ (at time $t = t_c$), as estimated by using data assimilation, and Figure 5d and 5f, respectively, show the predicted situation 10 and 20 s later, that is $\mathbf{u}_{n+10}^p$ and $\mathbf{u}_{n+20}^p$, in which $\Delta t = 1$ s. The synthesized distributions (i.e., the real distribution for this case) corresponding to Figure 5b,d,f are shown in Figure 5a,c,e, respectively. Thus, the situation in Figure 5a is estimated to be as shown in Figure 5b by using data assimilation, and Figure 5d,f shows the predictions from the assimilated distribution in Figure 5b. The precision of the predictions can be seen by comparing Figure 5c with 5d and Figure 5e with 5f. In Figure 5d and f, the distribution due to the fourth event is not predicted because the fourth event has not yet occurred at time t_c. The event occurs 4 s after t_c (at $t_c + 4$ s). We cannot predict the distribution due to future event. Predicting the occurrence of a future event is not a matter of EEW, but of earthquake prediction.

Application to Actually Observed Data

In this section, we explain the application of the method described above to actually observed data. As examples, we use the 2011 Tohoku earthquake (M_w 9.0), which occurred on a plate boundary east off Honshu island (the main island of Japan), and the 2004 Mid-Niigata Prefecture earthquake (M_w 6.7) which was a shallow inland event (focal depth, 13 km).

For actual application of the method, data must be transmitted in real time from many stations. At present, some stations transmit the data continuously in real time in Japan, but others record the waveform data using triggers. Although trigger-type stations do not send out waveform data in real time, some continuously transmit representative parameters of waveforms such as seismic intensity (Aoi *et al.*, 2008), because the data volume is much smaller than that of full waveforms. In Japan, the JMA scale is usually used for seismic intensity. Kunugi *et al.* (2008) proposed a method to estimate the time trace of JMA intensity, which is applicable in real time. In this article, taking into account the data availability of continuous data transmission, we use JMA intensity instead of waveforms. The JMA intensity is defined as the logarithm ($\log_{10}$) of the squared amplitude of the three-component accelerograms after band-pass filtering (high pass of 0.5 Hz, low pass of 10 Hz, and weight $(1/\text{freq})^{1/2}$, in which freq is frequency in hertz; see Hoshiba *et al.* (2010) and Hoshiba and Ozaki (2013) for detail). Because the energy density F in RTT is also proportional to the squared amplitude of band-pass-filtered seismograms, the relation between F and the JMA intensity can be expressed as $F = C10^{I_j(x,t)}$, in which C is constant independent of $\mathbf{x}$ and t, and $I_j(\mathbf{x}, t)$ is the time trace of JMA intensity measured at $\mathbf{x}$ in real-time manner. By defining F in this way, we can apply the proposed method to predict the JMA seismic intensity, as shown in the examples below.

To apply the method to actual observation, the difference in the site amplification factor must be corrected in real time. In this section, we first briefly explain the correction of the site amplification factor, and then we apply our proposed method to the example earthquakes.

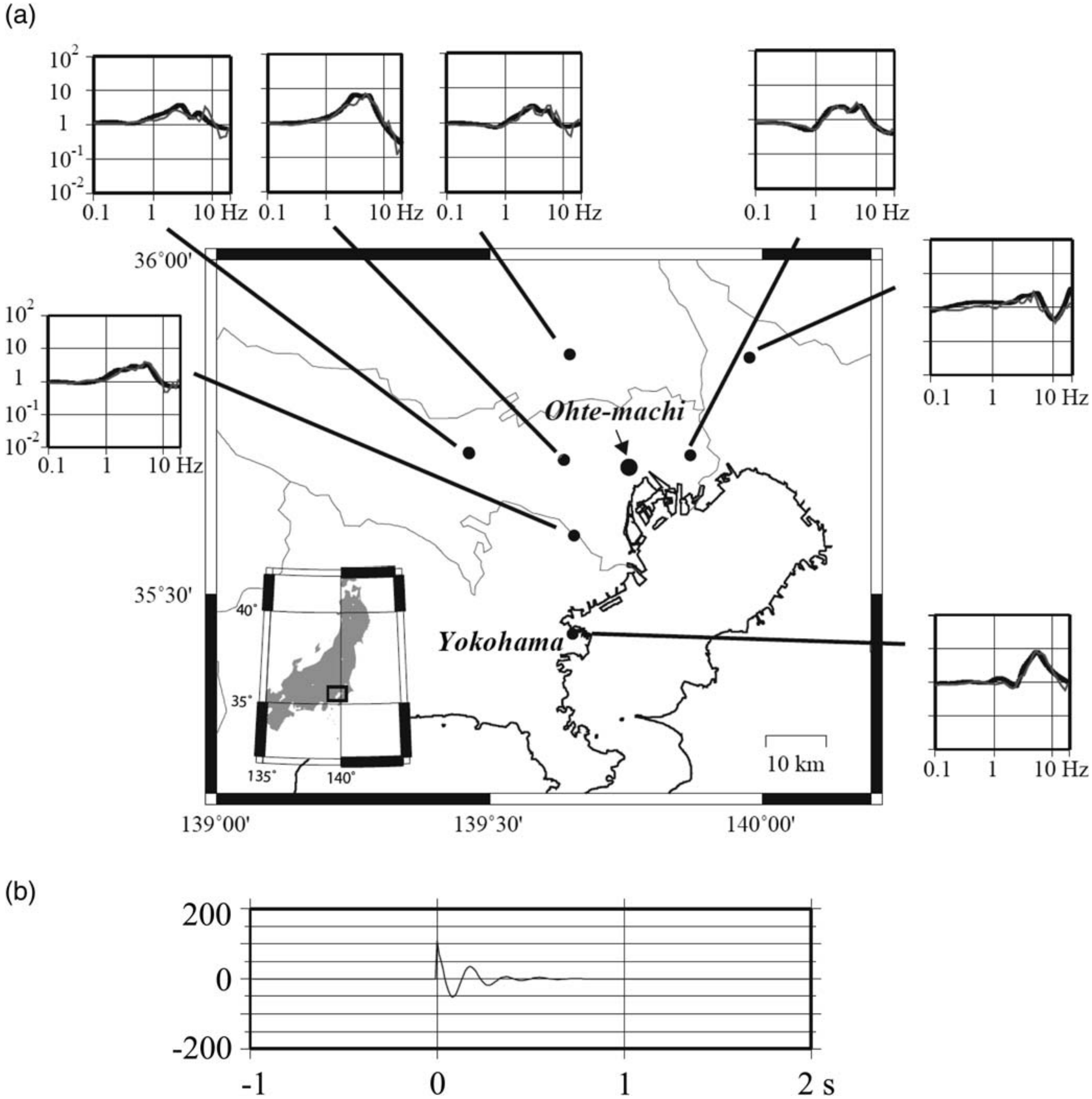

Figure 6. (a) Examples of frequency-dependent site amplification factors at various stations relative to that at Ohte-machi, Tokyo. The fine gray lines indicate the site amplification factors estimated from the observed waveforms of many past events. The bold black lines show the frequency dependence of the modeled infinite impulse response (IIR) filters. In this article, we focus on the 0.1–20 Hz frequency range, which has a great influence on JMA seismic intensity. (b) Example of the impulse response of the IIR filter in the time domain in which the site amplification at Yokohama relative to Ohte-machi is modeled. Reflecting the frequency dependence with a peak around 5 Hz, the time trace of the impulse response has several beats in a second with decreasing amplitude.

Real-time Correction of Site Amplification Factor

Site amplification is an important factor to determine seismic-wave amplitude in addition to source and propagation factors, and it usually depends on frequency. For the purpose of EEW, it is preferable to correct the frequency-dependent site amplification factor in real time. Recently Hoshiba (2013b) proposed using an infinite impulse response (IIR) filter to correct the site factor in real time. Aoki and Hoshiba (2014) estimated frequency-dependent site amplification factors at more than 1400 stations on Honshu and Shikoku (two main islands of Japan) and created their IIR filters, in which they used spectral ratios of neighbor stations far from the hypocenter to estimate the site factors. Figure 6 indicates some examples of

Δx	3 km	:	horizontal grid interval	
Δy	3 km	:	vertical grid interval	
Δt	1 s	:	time interval for data assimilation	
V_S	4 km/s	:	*S* wave velocity	
V_P/V_S	$\sqrt{3}$	:	V_P/V_S ratio	
g_0	0.002 km^{-1}	:	scattering strength	Attenuation
h_0	0.008 km^{-1}	:	absorption strength	Attenuation
a	7 km	:	correlation distance of the back ground error	
μ^b_{ij}	$\exp(-r^2/a^2)$	:	correlation type of the background error	
	r is the distance between the locations of the *i*-th grid and the *j*-th station			
μ^o_{kj}	0 for $k\neq j$, 1 for $k=j$	:	correlation of the observational error	
σ^o/σ^b	1	:	(observational error) / (background error)	

Figure 7. Parameters of the data assimilation and simulation of radiative transfer theory.

frequency-dependent site amplification factors relative to that at Ohte-machi, Tokyo. An example of the impulse responses of a filter is also shown. By applying the IIR filters, the difference due to the various site conditions are removed. The filtered-waveforms correspond to virtual observations in which the site conditions are replaced with that of Ohte-machi, Tokyo. From the filtered waveforms of the preceding 5 s (i.e., in range of $t-5$ s to t), we obtain $I_j(\mathbf{x}, t)$ using the Kunugi *et al.* (2008) technique.

The 2011 Tohoku Earthquake (M_w 9.0)

The 2011 Tohoku earthquake (M_w 9.0) occurred off the Pacific coast of Japan on 11 March 2011 and generated a huge tsunami that killed 18,958 people and left 2655 people missing (Fire Disaster Management Agency, Japan, 2014). Strong motion was observed over a wide area of northeastern Japan. Even at some stations in the Kanto district at epicentral distance exceeding 300 km, acceleration >1000 cm/s^2 was recorded. To explain the wide area of strong ground motion, some authors have proposed source models composed of multiple strong-motion generation areas (SMGAs): for example, Asano and Iwata (2012) proposed a source model with four SMGAs, and Kawabe *et al.* (2011) and Kurahashi and Irikura (2013) proposed models with five SMGAs. All of these studies identified at least two major SMGAs off Miyagi prefecture in the Tohoku district and several SMGAs off Fukushima prefecture southwest of the hypocenter.

We apply the proposed method to the data of the Tohoku earthquake. The parameters for data assimilation and for RTT are listed in Figure 7. Scattering strength g_0 and absorption strength h_0 are determined following Hoshiba (1993).

Figures 8 and 9 show the results of the application of the proposed method. Here, we apply data assimilation at 1 s intervals ($\Delta t = 1$ s). Figure 8a shows the observation of JMA seismic intensity in real-time manner, in which the difference in site amplification factors is removed by correcting the amplification relative to Ohte-machi, Tokyo. Figure 8a corresponds to $\mathbf{v}_n$ at various time steps n, and Figure 8b shows the distribution of seismic intensity after data assimilation (i.e., $\mathbf{u}^a_n$), in which all locations have virtually the same common site amplification factor as that of Ohte-machi, Tokyo. Thus, Figure 8b shows real-time shake maps. Although a standard ShakeMap is obtained by interpolation of the observed strength of ground motion after the earthquake (Wald *et al.*, 2006), taking into account the difference of site amplification, Figure 8b shows the distribution of ground motion at various lapse times after removing the difference in site amplification. Figure 8c,d shows the predictions of 10 and 20 s, respectively. Figure 9 shows the actually observed seismic intensity, along with the intensities predicted 5, 10, and 20 s in advance and the observed waveform of acceleration. As shown in Figure 8, at 130 s of elapse time, strong ground motion is observed to be propagating in northern Kanto, and the strong motion is predicted to reach Tokyo 20 s later. At 150 s of elapsed time, strong shaking is actually observed around Tokyo. As shown in Figure 9, however, this prediction is slightly overestimated: the seismic intensity (JMA scale) is predicted to be 5.7 at the 20 s prediction at 130 s of elapse time, and the intensity is actually observed to be 5.1 at 150 s of elapse time (i.e., overprediction by 0.6). The overprediction is improved with shortening the lead time: the 10 s prediction error is smaller than the 20 s prediction error, and the 5 s prediction error is much smaller.

Corrections for differences in site conditions are important for seeing the propagation of seismic waves in actual applications of the proposed method. If we apply the method without correcting for site differences, it is difficult to see the propagation of the seismic waves, because the waves seem to disappear in mountainous regions (hard-rock sites) and to emerge again when reaching basin regions (soft-rock sites).

Computation time is important for EEW application: it should be much less than the actual elapsed time in actual operation. In the proposed method, the computation time strongly depends on the number of grids I, the number of observation sites J, the number of particles M, and central processing unit (CPU) power. In the example shown in Figure 8, when we use $200 \times 100 = 20{,}000$ grids for I, 268 stations for J, and 10^6 for M, using a desktop PC (DELL Precision T3600), it takes ~0.5 s of CPU time for data assimilation for each time step ($\Delta t = 1$ s) and 0.2 s for prediction up to 20 s (i.e., a total of 0.7 s at each time step). This result suggests the computation time with this method is reasonably small for actual application to EEW.

Ⓔ Animation S1, available in the electronic supplement to this article, is an animation of Figure 8. Watching this animation of the real-time shake maps enables us to predict the

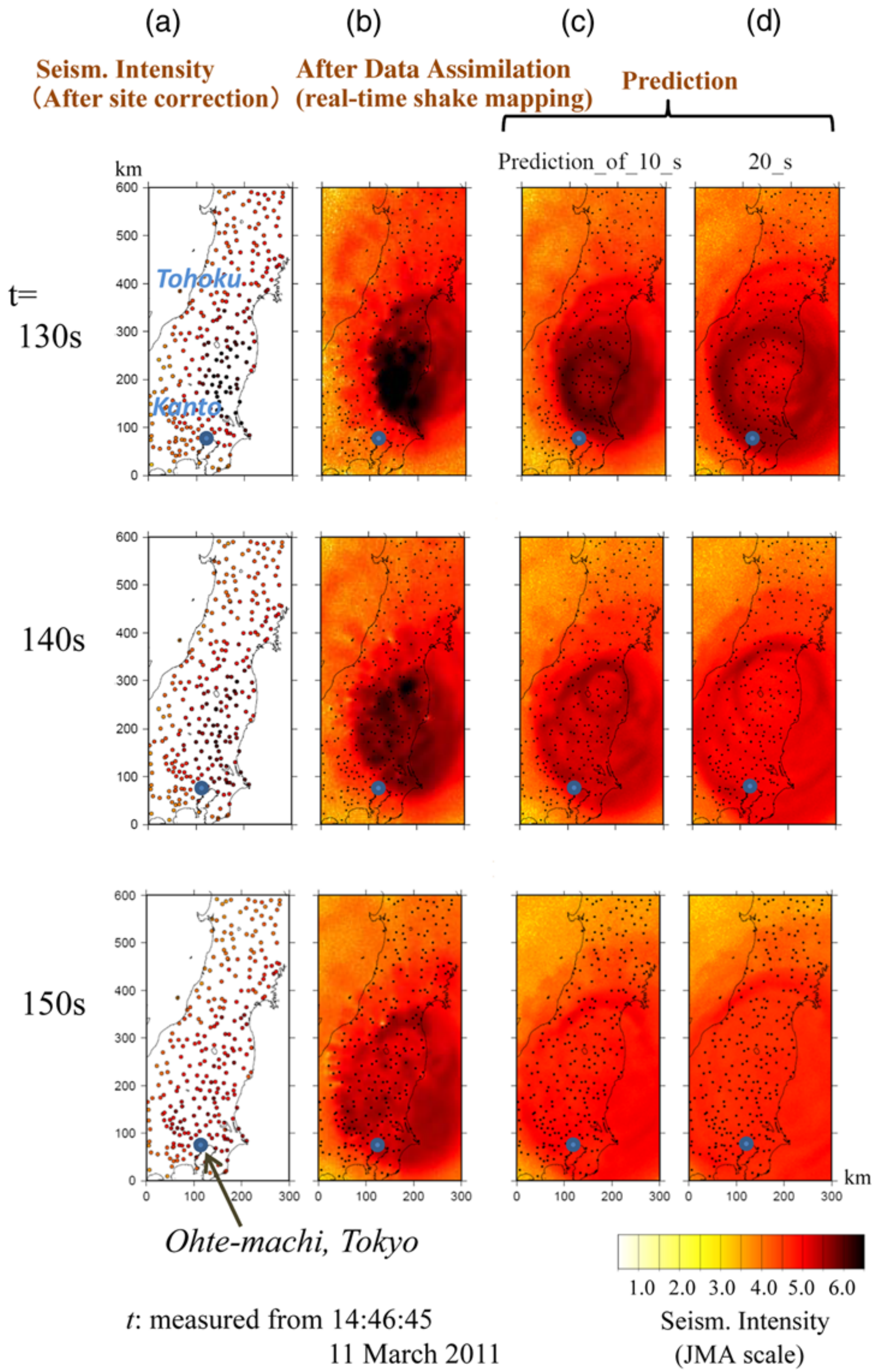

Figure 8. Example of prediction using data from the 2011 Tohoku earthquake (M_w 9.0): (a) seismic intensity on JMA scale after correction for site amplification factors; (b) the assimilated distributions (i.e., the real-time shake maps); and (c, d) the predictions of 10 and 20 s, respectively. The lapse times are measured from 14:46:45 11 March 2011 (Japan standard time). The color version of this figure is available only in the electronic edition.

future situation. The propagation of seismic waves approaching from outside the observation network is imaged following Huygen's principle, in which multiple simultaneous secondary sources produce a propagating wavefront with large radius. Strong ground motions repeatedly reach the Tohoku region, especially from the first two SMGAs off Miyagi prefecture. However, the first two SMGAs do not cause very strong shaking in the Kanto region. The strong ground motion that shakes the Kanto region is due to later ruptures. Even if the shaking is caused by the later ruptures, it is possible to

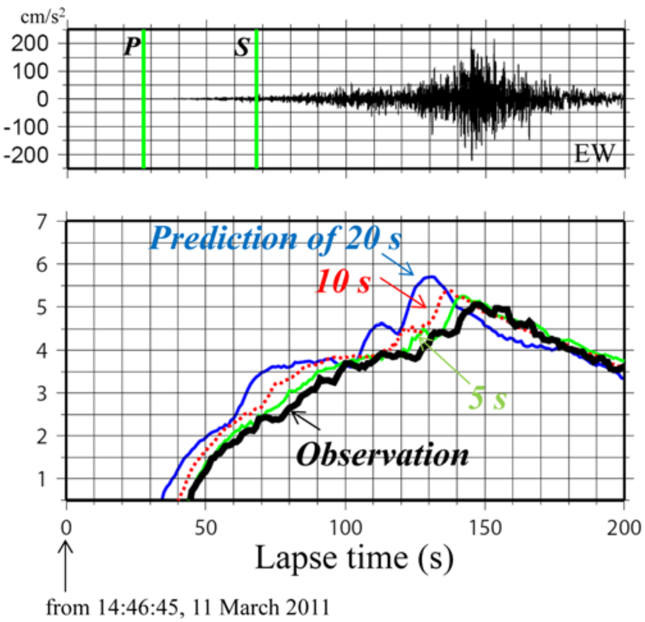

Figure 9. (Top) Acceleration due to the 2011 Tohoku earthquake, observed at Ohte-machi, Tokyo. Arrival times of the *P* and *S* phases are indicated. (Bottom) Observation of seismic intensity on the JMA scale measured in real-time manner by the technique of Kunugi *et al.* (2008) (bold line). Predictions of seismic intensity of 5, 10, and 20 s in advance are also shown. The color version of this figure is available only in the electronic edition.

predict it when we can observe its propagation as shown in the animation.

The 2004 Mid-Niigata Prefecture Earthquake (M_w 6.7)

The 2004 Mid-Niigata Prefecture earthquake (M_w 6.7) occurred in central Niigata prefecture, Japan, at a focal depth of 13 km on 23 October 2004. The earthquake caused tremendous damage in and around the focal area: 68 people were killed and more than 3100 houses collapsed as a result of the strong shaking (Fire Disaster Management Agency, Japan, 2009). A number of aftershocks followed the mainshock. We use this earthquake as an example of the application of the proposed method to multiple events.

Figure 10 shows the results of the data assimilation and prediction; Ⓔ its animation is available in the electronic supplement (Animation S2). Relatively strong ground motion propagates southeast toward Tokyo. As indicated in Figure 10b, at around 75 s of elapse time, the strong motion arrives at the Tokyo region. After the mainshock, at around 95 s, relatively weak motion spreads out around the source region; and, at around 105 and 115 s, relatively strong ground motion is again generated. Because of the many aftershocks, shaking is continuous at around the source region and intermittently reaches Tokyo (Ⓔ Animation S2). Even when the shakings are caused by many multiple events, it is possible to predict repeated shaking without identifying their sources by observing the seismic-wave propagation.

Discussion

The proposed method does not require estimating the source information, such as hypocenter location and M, for prediction of ground motion, which is different from many EEW techniques, including the current JMA EEW system. A dense observation network, however, is required. Even when applying the data assimilation technique, it is difficult to estimate precisely the distribution of ground motion without actual observations. When there are few stations around the target point (e.g., an isolated island, a peninsula, or a cape), precise estimation is not easy. In such cases, the source information may be a useful complement to the proposed method (Hoshiba, 2013a). When we estimate the source parameters (e.g., hypocenter, M, and origin time), we can image the distribution of ground motion due to P and S waves; the strength of the ground motion is distributed with concentric circles. The estimated distribution can be merged and replaced with the actual observation in regions with a dense observation network, and the resulting distribution can be used as $\mathbf{u}_n^a$. This interpolation method makes prediction of ground motion possible even where observations are sparse, when the hypocenter and M are well determined by the conventional approach.

Although the wavefield is observable at the ground surface when stations are densely deployed at the surface, the underground wavefield at depths of more than a few kilometers cannot be observed. In the previous section, we use 2D space for data assimilation and prediction. The 2D substitute corresponds to the assumption $f(x, y, z, t : \theta) = f(x, y, 0, t : \theta)$, in which x and y are the two horizontal axes and z is depth (ground surface is given by $z = 0$). Here, the spatial distribution of f does not depend on z, so energy propagates in the 2D image. Because of this assumption, the strength of ground motion tends to be slightly overpredicted, and the lead time to the arrival of strong ground motion may also be overpredicted. Energy propagates horizontally only with velocity V in 2D space, but with larger velocity (i.e., apparent velocity) in actual 3D space. Thus, strong ground motion may arrive earlier than predicted under the 2D assumption. Array analysis, which is a tool for discriminating P and S waves by comparing particle motion and propagation direction and for estimating apparent velocity, may make it possible to predict correctly the arrival time of strong ground motion. However, array analysis cannot be used to estimate the strength of the underground wavefield. Because many borehole observations deeper than a few kilometers are not realistic, assumptions are required for the strength of the underground wavefield to predict the strength of ground motion in the application of the proposed method even when many arrays are deployed. Handling the difference between the 2D and 3D spaces is an important subject for future advancement of this method.

For application of the data assimilation technique, we need to make estimates of the prior background error σ^b and the observational error σ^o. We assumed $\sigma^o/\sigma^b = 1$ in this article, as listed in Figure 7. The error ratio is determined

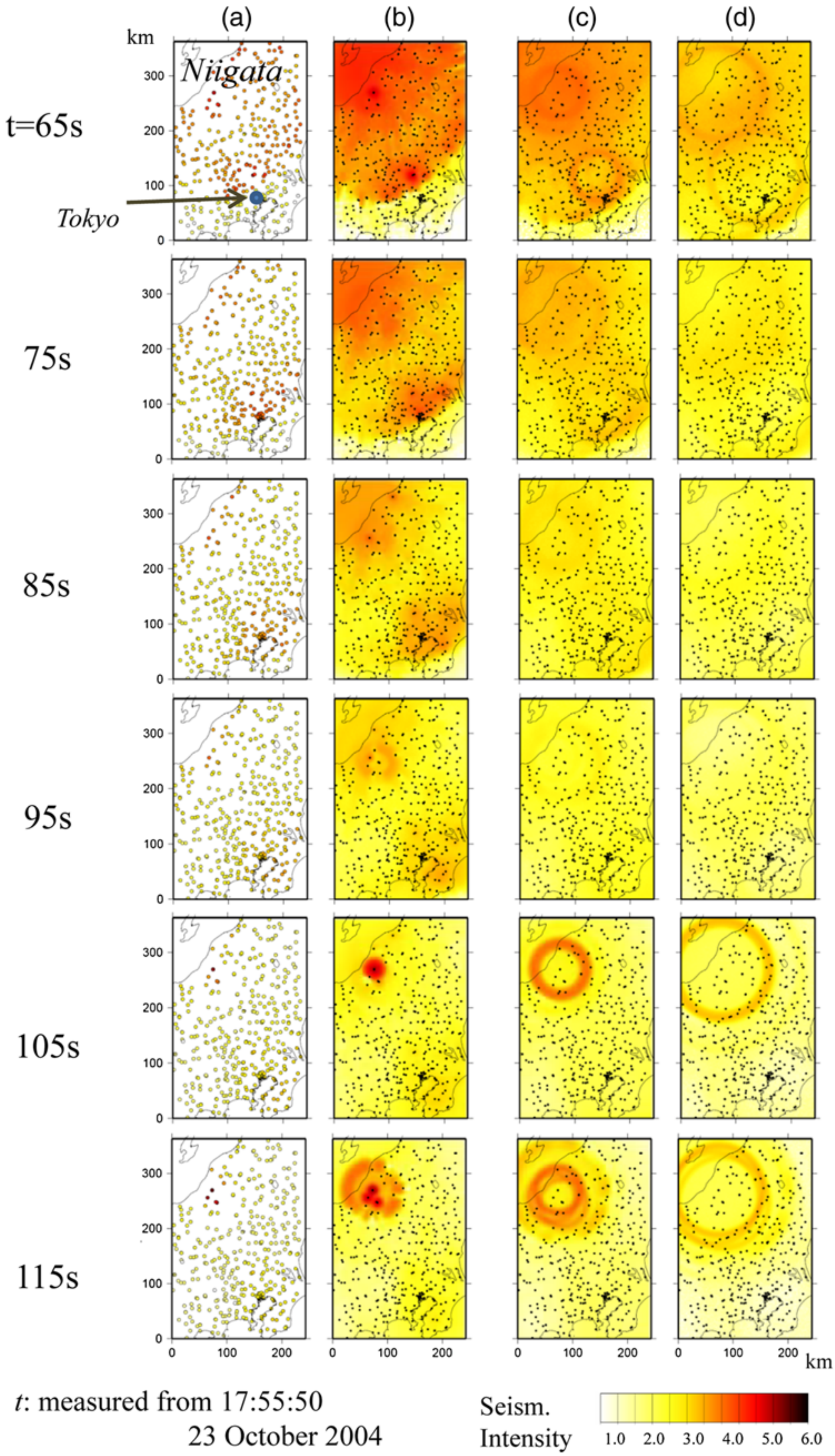

Figure 10. Example of predictions made using data from the 2004 Mid-Niigata Prefecture earthquake (M_w 6.7). (a) Seismic intensity on the JMA scales after correction for site amplification factors. (b) Assimilated distribution (i.e., the real-time shake maps). (c, d) Predictions of 10 and 20 s, respectively. The lapse times are measured from 17:55:50 23 October 2004 (Japan standard time). The color version of this figure is available only in the electronic edition.

from the reliabilities of observation and simulation. When observation is precise and is more reliable than the simulation of wave propagation, $\sigma^o/\sigma^b < 1$ is used; and, when simulation is precise, $\sigma^o/\sigma^b > 1$ is applied. Newly observed ground shaking is reflected to the estimation of wavefield more rapidly with decreasing σ^o/σ^b. From the viewpoint of prediction of ground shaking, therefore, too large σ^o/σ^b may result in underprediction at an early stage. On the other hand, if σ^o/σ^b is too small, it leads to jerky propagation, because small trivial fluctuations in observation are easily included. The appropriate assumption of σ^o/σ^b is an important key for precise estimation of the present wavefield in data assimilation and then for precise prediction.

Finally, we discuss again the difference between the proposed method and the conventional method based on source parameters.

Using the observed data from past to present, in the conventional method based on source parameters we look back to the oldest past situation from the view point of wave propagation. Not only is the future situation predicted, but postdiction of the past situation is performed from the oldest past situation. The period of time needed for estimation of the source parameters can be regarded as blind time with respect to EEW. In contrast, all data up to the present are used in the proposed method to estimate the present situation of wave propagation. Postdiction is not performed in the process.

In the conventional method based on source parameters, information about the very complicated space–time distribution of ground motion is first compressed to represent it by a limited number of parameters (usually five parameters: latitude, longitude, focal depth, origin time, and M), and then it is expanded again to predict ground motion. It is difficult to reconstruct completely the spatial distribution of ground motion even for the present situation: inevitably there are discrepancies between the predicted present situation and the actual present observation. As a result, even if estimation of the source parameters (e.g., hypocenter, M, and source extent) is precise, the prediction of ground motion is not necessarily similarly precise. In contrast, in the proposed method the actual present observation is reflected as much as possible in the estimate of the present situation. Discrepancies are minimized between the estimated present situation and the actual present observation by the data assimilation technique before we step forward to prediction.

Conclusion

We have proposed a method for real-time prediction of ground motion using data assimilation, real-time shake mapping, and simulation of wave propagation. This numerical shake prediction method is analogous to numerical weather prediction in meteorology. Although the proposed method requires a dense observation network, it makes it possible to predict ground motion without information about the earthquake hypocenter and magnitude. We have demonstrated that this method can precisely predict ground motion even when the extent of the fault rupture is large or when multiple events occur simultaneously. Thus, the proposed method addresses the issues raised by the 2011 Tohoku earthquake with regard to the JMA EEW system.

Data and Resources

Strong-motion acceleration data of K-NET and KiK-net were obtained from the National Research Institute for Earth Science and Disaster Prevention website (http://www.kyoshin.bosai.go.jp; last accessed May 2014), and strong-motion acceleration data of the Japan Meteorological Agency (JMA) were obtained from the JMA website (http:// www.data.jma.go.jp/svd/eqev/data/kyoshin/jishin/index.html; last accessed May 2014). The ShakeMap manual (Wald *et al.*, 2006) was obtained from the U.S. Geological Survey website (http://pubs.usgs.gov/tm/2005/12A01/pdf/508TM12-A1.pdf; last accessed June 2014).

Acknowledgments

We thank two reviewers and Associate Editor M. Gerstenberger for their careful reading and positive comments. We used waveform data from K-NET and KiK-net (National Research Institute for Earth Science and Disaster Prevention [NIED]) and from the Japan Meteorological Agency (JMA). We thank NIED and JMA for their efforts. Discussions with N. Hayashimoto were useful in this research, and he also helped us to prepare animations. M. Kamachi, Y. Fujii, N. Usui, and T. Toyoda helped us learn the data assimilation technique. Figures are produced using Generic Mapping Tools (Wessel and Smith, 1995). This research is partially supported by JSPS KAKENHI Grant Number 25282114 (Real-time prediction of earthquake ground motion: Method utilizing current observation).

References

Alcik, H., O. Ozel, N. Apaydin, and M. Erdik (2009). A study on warning algorithms for Istanbul earthquake early warning system, *Geophys. Res. Lett.* **36,** L00B05, doi: 10.1029/2008GL036659.

Aoi, S., T. Kunugi, S. Adachi, H. Nakamura, N. Morikawa, K. Obara, and H. Fujiwara (2008). Deployment of new strong-motion seismographs of KiK-net, *2008 Meeting of Japan Geoscience Union*, Chiba, Japan, 25–30 May 2008, Abstract S146–004.

Aoki, S., and M. Hoshiba (2014). Real-time site correction based on evaluating relative responses to common reference station for wide area network, *2014 Meeting of Japan Geoscience Union*, Yokohama, Japan, 28 April–2 May 2014, Abstract SSS28–05.

Asano, K., and T. Iwata (2012). Source model for strong ground motion generation in the frequency range 0.1–10 Hz during the 2011 Tohoku earthquake, *Earth Planets Space* **64,** 1111–1123, doi: 10.5047/eps.2012.05.003.

Awaji, T., M. Kamachi, M. Ikeda, and Y. Ishikawa (2009). *Data Assimilation: Innovation Combining Observation and Model*), Kyoto University Press, Kyoto, Japan, 284 pp., ISBN: 978-4-87698-797-9 (in Japanese).

Böse, M., T. H. Heaton, and E. Hauksson (2012). Real-time finite fault rupture detector (FinDer) for large earthquakes, *Geophys. J. Int.* **191,** 803–812, doi: 10.1111/j.1365-246X.2012.05657.x.

Böse, M., F. Wenzel, and M. Erdik (2008). PreSEIS: A neural network-based approach to earthquake early warning for finite faults, *Bull. Seismol. Soc. Am.* **98,** 366–382, doi: 10.1785/0120070002.

Cuéllar, A., J. M. Espinosa-Aranda, R. Suárez, G. Ibarrola, A. Uribe, F. H. Rodríguez, R. Islas, G. M. Rodríguez, A. García, and B. Frontana (2013). The Mexican Seismic Alert System (SASMEX): Its alert signals, broadcast results and performance during the M 7.4 Punta Maldonado earthquake of March 20th, 2012, in *Early Warning for Geological Disasters—Scientific Methods and Current Practice*, J. Zschau and F. Wenzel (Editors), Springer, Berlin, Germany, 71–87, doi: 10.1007/978-3-642-12233-0_4.

Fehler, M., M. Hoshiba, H. Sato, and K. Obara (1992). Separation of scattering and intrinsic attenuation for the Kanto-Tokai region, Japan, using measurements of S-wave energy versus hypocentral distance, *Geophys. J. Int.* **108,** 787–800.

Fire Disaster Management Agency, Japan (2009). Final report of the 2004 Mid-Niigata Prefecture earthquake (in Japanese), available at http://www.fdma.go.jp/data/010909231403014084.pdf (last accessed March 2015).

Fire Disaster Management Agency, Japan (2014). The 149th report of the 2011 Off the Pacific Coast of Tohoku earthquake (in Japanese), available at http://www.fdma.go.jp/bn/higaihou/pdf/jishin/149.pdf (last accessed August 2014).

Gasparini, P., and G. Manfredi (2013). Development of earthquake early warning systems in the European Union, in *Early Warning for Geological Disasters—Scientific Methods and Current Practice*, J. Zschau and F. Wenzel (Editors), Springer, Berlin, Germany, 89–101, doi: 10.1007/978-3-642-12233-0_5.

Gusev, A. A., and I. R. Abubakirov (1987). Monte-Carlo simulation of record envelope of a near earthquake, *Phys. Earth Planet. In.* **49,** 30–36.

Hoshiba, M. (1991). Simulation of multiple scattered coda wave excitation based on the energy conservation law, *Phys. Earth Planet. In.* **67,** 123–126.

Hoshiba, M. (1993). Separation of scattering attenuation and intrinsic absorption in Japan using the multiple lapse time window analysis of full seismogram envelope, *J. Geophys. Res.* **98,** 15,809–15,824.

Hoshiba, M. (1995). Estimation of nonisotropic scattering in western Japan using coda waves: Application of multiple nonisotropic scattering model, *J. Geophys. Res.* **100,** 645–657.

Hoshiba, M. (1997). Seismic coda wave envelope in depth dependent *S*-wave velocity structure, *Phys. Earth Planet. Int.* **104,** 15–22.

Hoshiba, M. (2013a). Real-time prediction of ground motion by Kirchhoff-Fresnel boundary integral equation method: Extended front detection method for earthquake early warning, *J. Geophys. Res.* **118,** 1038–1050, doi: 10.1002/jgrb.50119.

Hoshiba, M. (2013b). Real-time correction of frequency-dependent site amplification factors for application to earthquake early warning, *Bull. Seismol. Soc. Am.* **103,** 3179–3188, doi: 10.1785/0120130060.

Hoshiba, M., and T. Ozaki (2013). Earthquake early warning and tsunami warning of the Japan Meteorological Agency, and their performance in the 2011 Off the Pacific Coast of Tohoku earthquake (M_w 9.0), in *Early Warning for Geological Disasters—Scientific Methods and Current Practice*, J. Zschau and F. Wenzel (Editors), Springer, Berlin, Germany, 1–28, doi: 10.1007/978-3-642-12233-0_1.

Hoshiba, M., K. Iwakiri, N. Hayashimoto, T. Shimoyama, K. Hirano, Y. Yamada, Y. Ishigaki, and H. Kikuta (2011). Outline of the 2011 Off the Pacific coast of Tohoku earthquake (M_w 9.0)—Earthquake early warning and observed seismic intensity, *Earth Planets Space* **63,** 547–551, doi: 10.5047/eps.2011.05.031.

Hoshiba, M., O. Kamigaichi, M. Saito, S. Tsukada, and N. Hamada (2008). Earthquake early warning starts nationwide in Japan, *Eos Trans. AGU* **89,** 73–74, doi: 10.1029/2008EO080001.

Hoshiba, M., K. Ohtake, K. Iwakiri, T. Aketagawa, H. Nakamura, and S. Yamamoto (2010). How precisely can we anticipate seismic intensities? A study of uncertainty of anticipated seismic intensities for the earthquake early warning method in Japan, *Earth Planets Space* **62,** 611–620, doi: 10.5047/eps.2010.07.013.

Hoshiba, M., A. Rietbrock, F. Scherbaum, H. Nakahara, and C. Harberland (2001). Scattering attenuation and intrinsic absorption using uniform and depth dependent model—Application to full seismogram envelope recorded in northern Chile, *J. Seismol.* **5,** 157–179.

Hsiao, N. C., Y. M. Wu, T. C. Shin, L. Zhao, and T. L. Teng (2009). Development of earthquake early warning system in Taiwan, *Geophys. Res. Lett.* **36,** no. L00B02, doi: 10.1029/2008GL036596.

Irikura, K., and S. Kurahashi (2011). Improvement of earthquake early warning taking rupture extent into account, *Proceedings of ERI Meeting of Rapid Analysis and Prediction of Seismic Ground Motion*, Tokyo, Japan, 8–9 September 2011 (in Japanese).

Ishimaru, A. (1997). *Wave Propagation and Scattering in Random Media*, IEEE press, New York, 574 pp.

Kalnay, E. (2003). *Atmospheric Modeling, Data Assimilation and Predictability*, Cambridge University Press, Cambridge, United Kingdom, 341 pp.

Kawabe, H., K. Kamae, and H. Uebayashi (2011). Source model of the 2011 Tohoku-Chiho Taiheiyo-Oki earthquake, *Seismol. Soc. Japan* (Fall Meet.), Abstract B22-05 (in Japanese).

Kunugi, T., S. Aoi, H. Nakamura, H. Fujiwara, and N. Morikawa (2008). A real-time processing of seismic intensity, *Zisin 2*, **60,** 243–252 (in Japanese).

Kurahashi, S., and K. Irikura (2013). Short-period source model of the 2011 M_w 9.0 Off the Pacific Coast of Tohoku earthquake, *Bull. Seismol. Soc. Am.* **103,** no. 2B, 1373–1393, doi: 10.1785/0120120157.

Kuyuk, H. S., R. M. Allen, H. Brown, M. Hellweg, I. Henson, and D. Neuhauser (2014). Designing a network-based earthquake early warning algorithm for California: ElarmS-2, *Bull. Seismol. Soc. Am.* **104,** 162–173, doi: 10.1785/0120130146.

Liu, A., and M. Yamada (2014). Bayesian approach for identification of multiple events in an early warning system, *Bull. Seismol. Soc. Am.* **104,** 1111–1121, doi: 10.1785/0120130208.

Sato, H., M. C. Fehler, and T. Maeda (2012), *Seismic Wave Propagation and Scattering in the Heterogeneous Earth*, Second Ed., Springer, Berlin, Germany, 494 pp., doi: 10.1007/978-3-642-23029-5.

Utsu, T. (2001). *Seismology*, Third Ed., Kyoritsu Shuppan, Tokyo, Japan, 376 pp. (in Japanese).

Wald, D., B. C. Worden, V. Quitoriano, and K. L. Pankow (2006). *ShakeMap Manual: Technical Manual, Users Guide, and Software Guide*, USGS web site, 156 pp, http://pubs.usgs.gov/tm/2005/12A01/pdf/508TM12-A1.pdf (last accessed June 2014).

Wessel, P., and W. H. F. Smith (1995). New version of the Generic Mapping Tool released, *Eos Trans. AGU* **76,** 329.

Yamada, M. (2013). Estimation of fault rupture extent using near-source records for earthquake early warning, in *Early Warning for Geological Disasters—Scientific Methods and Current Practice*, J. Zschau and F. Wenzel (Editors), Springer, Berlin, Germany, 1–28, doi: 10.1007/978-3-642-12233-0_2.

Yoshimoto, K. (2000). Monte Carlo simulation of seismogram envelopes in scattering medium, *J. Geophys. Res.* **105,** 6153–6161, doi: 10.1029/1999JB900437.

Meteorological Research Institute
Japan Meteorological Agency
Nagamine 1-1
Tsukuba 305-0052, Japan
mhoshiba@mri-jma.go.jp

Manuscript received 19 September 2014;
Published Online 5 May 2015